

AD-A262 802



ATION PAGE

Form Approved
OMB No. 0704-0188

2

This report contains information which is classified "Secret" under Executive Order 12958, Section 1.5, and is exempt from automatic downgrading and declassification. It is intended for use by the Department of Defense and its agencies only. It is not to be distributed outside the Department of Defense and its agencies. It is not to be used for any other purpose without the express written permission of the Department of Defense. It is not to be used for any other purpose without the express written permission of the Department of Defense.

1. AGENCY USE ONLY (Leave blank)		2. REPORT DATE March 9, 1993	3. REPORT TYPE AND DATES COVERED Reprint	
4. TITLE AND SUBTITLE Inelastic and Ballistic Processes Resulting From CsF-Ar Collisions			5. FUNDING NUMBERS PE 63220C PR S321 TA 13 WU 01	
6. AUTHOR(S) Ramesh D. Sharma, Joseph M. Sindoni*				
7. PERFORMING ORGANIZATION NAME(S) AND ADDRESS(ES) Phillips Lab/GPOS 29 Randolph Road Hanscom AFB, MA 01731-3010			8. PERFORMING ORGANIZATION REPORT NUMBER PL-TR-93-2049	
9. SPONSORING MONITORING AGENCY NAME(S) AND ADDRESS(ES)			10. SPONSORING MONITORING AGENCY REPORT NUMBER	
11. SUPPLEMENTARY NOTES *Yap Analytics, Inc. Lexington, MA 02173 Reprinted from J. Chem. Phys. 98 (2), 15 January 1993				
12. DISTRIBUTION AVAILABILITY STATEMENT Approved for public release; Distribution unlimited			13. DISTRIBUTION STATEMENT UNCLASSIFIED	
12. ABSTRACT <p>This paper continues the study of inelastic and ballistic collisions for the CsF-Ar system using the impulse approximation (IA). The IA expresses the atom-diatom potential as the sum of the two atom-atom potentials. The atom-atom interaction is approximated by a hard core potential, and the laboratory differential cross sections are calculated for an initial relative translational energy of 1.0 eV as a function of the laboratory recoil velocity of CsF. The calculated differential cross sections are in excellent agreement with the experimental measurements for all eight laboratory scattering angles for which the data are available.</p>				
14. SUBJECT TERMS Inelastic, Ballistic, Collisions			15. NUMBER OF PAGES 16	
			16. PRICE CODE	
17. SECURITY CLASSIFICATION OF REPORT UNCLASSIFIED	18. SECURITY CLASSIFICATION OF THIS PAGE UNCLASSIFIED	19. SECURITY CLASSIFICATION OF ABSTRACT UNCLASSIFIED	20. LIMITATION OF ABSTRACT SAR	

DTIC
SELECTED
MAR 16 1993
S B D

Inelastic and ballistic processes resulting from CsF-Ar collisions

Ramesh D. Sharma

*Phillips Laboratory, Optical Environment Division (GPOS), Hanscom Air Force Base,
Massachusetts 01731-5000*

Joseph M. Sindoni

Yap Analytics Inc., Lexington, Massachusetts 02173

(Received 29 June 1992; accepted 30 September 1992)

This paper continues the study of inelastic and ballistic collisions for the CsF-Ar system using the impulse approximation (IA). The IA expresses the atom-diatom potential as the sum of the two atom-atom potentials. The atom-atom interaction is approximated by a hard core potential, and the laboratory differential cross sections are calculated for an initial relative translational energy of 1.0 eV as a function of the laboratory recoil velocity of CsF. The calculated differential cross sections are in excellent agreement with the experimental measurements for all eight laboratory scattering angles for which the data are available. While the calculated results show no significant dependence on the initial relative velocity or on the initial vibrational quantum number of CsF, they do show a systematic variation with the initial rotational quantum number—the ballistic effect is more pronounced than that observed experimentally for initial quantum rotational numbers less than 30 and is not pronounced enough for rotational quantum numbers more than 100. Two mechanisms give rise to the ballistic peak. The first one is dominant when the laboratory scattering angle is equal, or nearly equal, to the laboratory angle of the centroid velocity. This mechanism transfers almost all of the relative translational energy into the internal energy of the diatom and magnifies the center-of-mass (c.m.) differential cross section almost a million times. This is due to a singularity in the Jacobian at very small c.m. recoil velocities, which physically means that a small solid angle in the laboratory frame can collect the signal from all 4π steradians in the c.m. frame. The second mechanism producing the ballistic peak, also determining the smallest and the largest laboratory scattering angles, is the rainbowlike singularity called edge effect. This mechanism becomes operative when the recoil velocity of the alkali halide in the c.m. frame is perpendicular to its recoil velocity in the laboratory frame. While the dynamics of the collision leads to a conversion of the proper amount of relative translational energy into internal energy of the diatom, the kinematic singularities mentioned above magnify the relevant c.m. differential cross sections leading to the observed ballistic effect. The ballistic effect, therefore, should be observable for any two collision partners under appropriate circumstances. The simple atom-diatom potential reproduces the experimental results very well, because (i) for inelastic scattering, the experimental observations correspond to large center of mass scattering angles for which the attractive part of the potential makes little contribution to the scattering process, (ii) for ballistic scattering, only the repulsive portion of the potential can cause a large amount of energy exchange between the relative translational and the internal degrees of freedom, and (iii) the calculated cross sections are insensitive to the details of the repulsive portion of the potential. A number of consequences of the theory, including the conclusion that the alkali halide beam in the experiments is rotationally unrelaxed, are discussed.

1. INTRODUCTION

In a series of experiments, Herschbach and co-workers¹⁻³ have measured the differential cross sections for the scattering of CsX (X = F, I) by Ar as a function of the laboratory recoil velocity of CsX by crossing the two beams, at a right angle to each other, at a relative translational energy of about 1.0 eV. In addition to a peak observed around the elastically scattered CsX (pseudoelastic peak, formerly called the elastic peak⁴), another peak, almost as strong as the pseudoelastic peak and named the ballistic peak, was observed in the vicinity of the recoil velocity corresponding to the motion of the center of mass.

Obviously, those molecules that constitute the ballistic peak have a substantial fraction of their relative translational energy converted into internal energy during the collisions. A theory of the ballistic effect is thus a theory of collisions during which a large fraction of the relative translational energy is converted into internal energy. The pseudoelastic peak observed in the experiments¹⁻³ corresponds to large angle scattering in the center of mass (c.m.) frame. The theory of the collisions comprising the pseudoelastic peak, also under consideration here, is therefore a theory of large angle elastic and inelastic scattering.

A model for the inelastic and ballistic transitions for the CsF-Ar system constructed earlier⁴ produces excellent



93-05367

280 51 8 86

agreement with the experimentally measured differential cross section as a function of the laboratory recoil velocity of CsF at the laboratory scattering angles of 30° and 60° . According to this model, the inelastic (ballistic) collisions results when Ar strikes the Cs (F) end of CsF. The inelastic collisions involve modest change in the rotational quantum number ($\Delta j=50$); the ballistic collisions, on the other hand, to conserve angular momentum and energy, must involve large changes in the rotational quantum number (Δj up to about 200). Our model for the ballistic and large angle inelastic collisions has been able to give a quantitative explanation of the experimental observations of the CsF-Ar system, but it has not been able to explain the ballistic effect observed in the CsI-Ar system. Our model, however, has pointed out that the ballistic effect should not be observed in the I_2 -Ar system at about 1 eV relative translational energy because the I_2 beam is rotationally cold (rotational temperature $\sim 250^\circ$ for the I_2 beam vs $\sim 1000^\circ$ for the CsI beam), a prediction in agreement with the experimental results. The present theory has, in addition, predicted a ballistic peak for the I_2 -Ar system at relative translational energy of about 0.12 eV.⁴ This prediction of our model is in contrast to the prediction of an earlier model⁵ of atom-diatom collisions, which concludes that only about 25% of the initial relative translational energy should be converted into internal energy during an Ar- I_2 encounter, independent of the initial internal energy of the diatom or the atom-diatom relative translational energy. The same model⁵ predicts a transfer of about 96% of the relative translational energy into internal degrees of freedom during an Ar-FCs encounter, again independent of the initial internal energy of the diatom or the atom-diatom relative translational energy. It was pointed out earlier⁴ that when the laboratory scattering angle is the same, or nearly the same, as the laboratory angle of the c.m. velocity, a transfer of more than 96% of the relative translational energy into internal degrees of freedom is required to observe a ballistic effect. It will be shown later, in this article, that when the laboratory scattering angle is much larger than, or much smaller than, the laboratory angle of the c.m. velocity, a transfer of a mere 75% of the relative translational energy into internal degrees of freedom may lead to a ballistic effect. Again this is in conflict with the earlier model⁵ of impulsive collisions. Our model, since it has not explained all the pertinent experimental observations, is only the first step in fully understanding the mystery of ballistic collisions. Nevertheless, by virtue of the excellent agreement between the calculated and the measured results for the CsF-Ar system, the predictions it has made, and the experiments it has suggested, our model represents a valuable first step. For this reason it is considered appropriate to present a more complete theory for the CsF-Ar system, expanding on the previous results as well as presenting new ones.

Before presenting the detailed theory of the ballistic effect, it is necessary to discuss the transformation of the differential cross sections from the c.m. frame to the laboratory coordinates. This transformation is an important link bridging the results calculated in the c.m. frame to the

experimental results measured, of course, in the laboratory frame. Section II discusses this transformation, which is derived in the Appendix. Section III gives a brief account of the impulse approach (IA) for the atom-diatom collisions with a special emphasis on the part-classical (previously called "semi-classical") formalism. The calculation is still fully quantum, but by treating the two-body dynamics classically it is possible to save a great deal of computing time without appreciable loss of accuracy. Section IV briefly describes the computational procedures used. Section V discusses the two mechanisms leading to the ballistic peak. The results of the calculation are compared with the experimental measurements in Sec. VI. Our state-resolved three dimensional fully quantum calculation is examined in greater detail in Sec. VII and some of its more interesting consequences are pointed out. Concluding remarks and lessons learned comprise the last section, Sec. VIII.

II. TRANSFORMATION OF THE DIFFERENTIAL CROSS SECTION FROM THE CENTER OF MASS TO THE LABORATORY SYSTEM

The transformation between the c.m. and the laboratory coordinate systems has been the subject of several studies.⁶⁻⁸ We give a particularly simple derivation of the Jacobian for inelastic scattering. We then use this derivation as the starting point for the discussion of singularities and connect it with the previous work on the ballistic collisions.

The differential cross section in the laboratory coordinate system $\sigma_L(\theta_L, \phi_L)$ is related to the differential cross section in the center of mass coordinate system $\sigma(\theta, \phi)$ by the relation

$$\sigma_L(\theta_L, \phi_L) = \lim_{\Delta\Omega_L \rightarrow 0} \int_{\Omega_m}^{\Omega_M} \sigma(\theta, \phi) d\Omega / \Delta\Omega_L, \quad (1)$$

where θ, ϕ are the polar and the azimuthal angles and Ω is the solid angle in the c.m. coordinate system; the subscript L indicates that the angles are measured in the laboratory coordinate system. $\Omega_{M(m)}$ denotes the maximum (minimum) c.m. solid angle corresponding to laboratory solid angles $\Omega_L \pm \Delta\Omega_L$. Defining

$$\left(\frac{v_2'}{\omega_2'}\right)^2 \equiv \gamma^2, \quad (2)$$

and taking the limit as $\Delta\Omega_L$ approaches zero, the expression for the Jacobian is written as

$$\sigma_L(\theta_L, \phi_L) = \left| \frac{d\Omega_L(\theta_L, \phi_L)}{d\Omega(\theta, \phi)} \right|^{-1} \sigma(\theta, \phi), \quad (3)$$

where θ, ϕ , and θ_L, ϕ_L are polar and azimuthal scattering angles in the c.m. frame and the laboratory frame, respectively. Defining $\gamma \equiv (v_{c.m.}/\omega_2')$ as the ratio of the velocity of the centroid in the laboratory frame to the recoil velocity of the observed particle in the c.m. frame, we show, in the Appendix,

$$\left| \frac{d\Omega_L(\theta_L, \phi_L)}{d\Omega(\theta, \phi)} \right|^{-1} = \frac{2\gamma_1^3}{|1 + \gamma_1^2 - \gamma^2|} = \frac{\gamma_1^2}{|(\hat{\omega}_2' \cdot \hat{\omega}_2')|}, \quad (4)$$

where $\hat{\omega}_2' \cdot \hat{\omega}_2'$ is the cosine of the angle between the recoil velocities of the species detected in the laboratory and the c.m. frames. It is shown in the Appendix that Eq. (4) is identical to the one given by Schiff⁹ when one of the particles is initially stationary. This expression becomes infinite when ω_2' approaches zero, i.e., when the c.m. recoil velocity becomes very small, and also when the c.m. and the laboratory recoil velocities are perpendicular.

When ω_2' approaches zero, the direction of v_2' , the laboratory recoil velocity, coincides with that of the centroid velocity, $v_{c.m.}$. It is pointed out in the Appendix that in this case the Jacobian becomes a constant and is simply equal to $4\pi/\Delta\Omega_L$, $\Delta\Omega_L$ being the laboratory solid angle seen by the detector. For a 0.25° wide detector, the Jacobian is equal to 8.4×10^5 . Herein lies part of the mystery of the ballistic effect! A millionfold enhancement of the cross sections for the processes that lead to the conversion of almost all of the relative translational energy into internal energy causes very small cross sections in the c.m. frame to stand out in the laboratory frame. This hypothesis is the basis of the proposal for the production of the state-selected and velocity-selected molecular beams.⁴

When the laboratory and c.m. recoil velocities are perpendicular, the Jacobian given above again becomes infinite. It is shown in the Appendix that for a given final vibrational-rotational state, i.e., for constant magnitude of ω_2' , the laboratory scattering angle as a function of c.m. scattering angle goes through a maximum (minimum) when the laboratory scattering angle is greater (smaller) than the centroid velocity angle θ_2 . An increase (decrease) in the c.m. scattering angle leads to a decrease (increase) in the laboratory scattering angle. The situation encountered here is the same as that encountered in the study of rainbows¹⁰ where the extremum in the deflection function as a function of impact parameter leads to infinite classically calculated differential cross section. These two rainbowlike singularities, called the edge effect,¹¹ correspond to a lower and an upper bound for the laboratory scattering angle for a given final vibrational-rotational state. The rainbowlike singularities encountered here are due to kinematic effects and are distinct from the rainbows due to the dynamical effects discussed previously.¹²

In the Appendix the Jacobian for the edge effect is shown to be equal to

$$\left| \frac{d\Omega_L}{d\Omega} \right|^{-1} \equiv \left| \frac{\sin \theta_L \Delta\theta_L d\phi_L}{\sin(\theta + \theta_1 - \theta_2) \Delta\theta d\phi} \right|^{-1} \cong \left| \frac{8\gamma_1^3}{\Delta\theta_L} \right|^{1/2}, \quad (5)$$

where the angle $\Delta\theta_L$ is the width of the polar angle of the detector. The Jacobian given by Eq. (5) for $\gamma_1 \approx 5$ and $\Delta\theta_L = 0.250$ deg can have a value roughly between 100 and 1000 depending upon the laboratory scattering angle, i.e., it can have a value between 4 and 40 times that given by γ_1^2 alone. This effect is not as dramatic as that due to resonant transfer of energy from relative translational motion into rotational and vibrational motion of the diatom. However,

in this case the combined contributions from different transitions can lead to an equally strong ballistic peak.

III. ATOM-DIATOM IMPULSE FORMALISM

The complete formulation of the impulse approach to atom-diatom collisions was given earlier.¹³ Here we give a brief outline for completeness with an emphasis on the part-classical approximation to the exact equations. In this formulation the dynamics of two-body collisions is treated classically while the remainder of the calculation is carried out using quantum mechanics. It has been found that this procedure leads to substantially reduced computing time while the error introduced has never been found to exceed 10%. In the present calculation more than 100 000 differential cross sections had to be computed; the use of this approximation has kept the computation time manageable.

The interaction potential of the atom-diatom system in the impulse formulation is the sum of the spherically symmetric atom-atom potentials, i.e.,

$$V(y_1, y_2) = V_1(y_1) + V_2(y_2), \quad (6)$$

where V_i and y_i are, respectively, the interaction potential and the distance between the incident atom and atom j of the diatom. The distance between the incident atom 3 and atoms 1 and 2 of the diatom is written as

$$y_s = [r^2 + 2\alpha_s r y_3 \cos \gamma_s + (\alpha_s y_3)^2]^{1/2}, \quad (7)$$

where $s=1,2$ and r is the distance between the atom and the center of mass (c.m.) of the diatom; y_3 is the internuclear distance of diatom 1-2,

$$\alpha_s = (-1)^s m_j / (m_1 + m_2), \quad (8)$$

m_s is the mass of the spectator atom, and γ_s is the angle between the internuclear axis y_3 and the line r joining the atom to the c.m. of the diatom. Eigenfunctions $\psi_{v,j,m}$ of the Hamiltonian for the diatomic molecule

$$H_{\text{DIATOM}} = \frac{q_3^2}{2\mu_{12}} + V_3(y_3) \quad (9)$$

are the wave functions for the vibrational and rotational motion of the diatom. The momenta are written in the Jacobi notation; \mathbf{p}_a is the momentum of particle a with respect to the c.m. of bc and \mathbf{q}_a is the relative momentum of particles bc . Similarly, \mathbf{r}_a is the distance of atom a from the c.m. of bc , y_a is the distance between b and c , and V_3 is the intramolecular potential of the diatom 1-2. μ_{ij} is the reduced mass of the atoms i and j , while the reduced mass of a and bc is written as μ_a .

The Watson expansion, a multiple-collision expansion of the three-body T matrix, is written as¹⁴

$$T = T^{(1)} + T^{(2)} + T^{(1)}G_3T^{(2)} + T^{(2)}G_3T^{(1)} + \dots \quad (10)$$

where $T^{(i)}$ is the three-body transition matrix describing the collision of the incident atom with atom j of the diatom, i being the spectator atom. G_3 is the propagator corresponding to the unperturbed Hamiltonian H_0 , viz.,

$$H_0 = \frac{p_3^2}{2\mu_3} + H_{\text{DIATOM}} \quad (11)$$

and,

$$G_3(z) = (z - H_0 + i\eta)^{-1} \quad (12)$$

The first two terms on the right-hand side of Eq. (10) are the single-collision terms. These terms are obtained by summing all the diagrams involving the collision of the incident atom with atom 1 or atom 2. The graphs representing the collision of the incident atom with atom 1 (2) followed by further collisions of the incident atom with atom 1 (2) are contained in these terms.¹⁴ The next two terms are the double-collision terms and are obtained by summing all the diagrams involving the collision of the incident atom first with atom 1 (2) followed by collision with atom 2 (1).¹⁴ In the impulse calculation only the first two terms, i.e., only the single collision terms, are retained.

We can write the differential cross section for scattering from initial state i to final state f as

$$\frac{d\sigma}{d\Omega} (i \equiv v_j p_3, f \equiv v'_j, p'_3; q) = \frac{p'_3}{p_3} (2j+1)^{-1} \mu_3^2 \left(\frac{2\pi}{\hbar} \right)^4 |T_{if}|^2, \quad (13)$$

where the scattering angle θ and momentum transfer vector \mathbf{q} are related by

$$q^2 = (p'_3)^2 + (p_3)^2 - 2p_3 p'_3 \cos \theta, \quad (14)$$

and,

$$|T_{if}|^2 = \sum_{m,m'} |\langle \phi'_3 | T | \phi_3 \rangle|^2, \quad (15)$$

ϕ_3 and ϕ'_3 being the eigenfunctions of H_0 in the initial and final states, respectively, and,

$$T_{if}(\mathbf{q}) = \left(\sum_{s=1,2} T_{if}^{(s)}(\mathbf{q}) \right). \quad (16)$$

The two terms on the right-hand side of Eq. (16) are the single collision terms. When the incident atom collides with one of the atoms of the diatom, the other atom, the one not participating in the collision process, is termed the spectator. For this reason the impulse calculation is also called the quantum mechanical spectator model. We recall that

$$\langle \phi'_3 | T^{(s)}(\mathbf{q}) | \phi_3 \rangle = \int d\mathbf{y}_3 \phi_3^* (\mathbf{y}_3) \exp(-i\alpha\mathbf{q} \cdot \mathbf{y}_3) \times \Psi^{(s)}(\mathbf{y}_3), \quad (17)$$

where

$$\Psi^{(s)}(\mathbf{y}_3) \equiv (2\pi)^{-3/2} \int d\mathbf{q}_3 \exp(-i\mathbf{q}_3 \cdot \mathbf{y}_3) \times \langle \mathbf{q}'_3 | t^{(s)} | \mathbf{q}_3 \rangle \phi(\mathbf{q}_3) \quad (18)$$

is the wave function of the diatom modified by the two-body scattering process. To develop a feeling for the nature

of $\Psi^{(s)}(\mathbf{y}_3)$, it is useful to look at the two-body t matrix as an operator in the momentum space which modifies the diatom wave function $\phi(\mathbf{q}_3)$. Equation (18) transforms the modified wave function back to the coordinate space. If one recalls that the center of mass acquires a momentum equal to $\alpha\mathbf{q}$ during the collision when s is the spectator atom, Eq. (17) may be looked upon as the overlap integral of the final-state wave function with the initial-state wave function that is modified by the collision. This view also connects the impulse approach discussed here with the theory of transitions due to sudden perturbations, e.g., atomic transitions accompanying beta ray emission.¹⁵

It was mentioned earlier that we will evaluate the two-body t matrix in Eq. (18) using classical mechanics. In classical mechanics, a collision between two hard spheres leads to the reversal of the component of the momentum normal to the surfaces of the two spheres at the point of contact, while the other two components of the momentum remain unchanged.¹⁶ In other words, if a momentum change \mathbf{q} occurs during the collision, the initial momentum $-\mathbf{q}/2$ becomes the final momentum $+\mathbf{q}/2$, while the components of momentum perpendicular to \mathbf{q} remain unchanged. Further, the transverse components of the momentum, which in classical mechanics do not enter the equations of motion, may have any value. It was shown earlier¹³ that this result also holds for scattering using the impulse approach, provided the scattering angle is larger than about 15° . This amounts to evaluating Eq. (18) by setting the components of \mathbf{q}_3 along \mathbf{q} equal to

$$\mathbf{q}_3 \cdot \hat{\mathbf{q}} = -(\alpha\mathbf{q}/2) + \mu_{12}\Delta\epsilon/(\alpha\mathbf{q}), \quad (19)$$

where $\hat{\mathbf{q}}$ is a unit vector along the direction of the transferred momentum and $\Delta\epsilon$ is the difference in internal energy of the diatom between the final and the initial states. The components of \mathbf{q}_3 perpendicular to \mathbf{q} are set equal to zero. It was also pointed out earlier¹³ that to evaluate the two-body t matrix for a fixed value of \mathbf{q}_3 , the momentum due to the vibrational and rotational motion of the diatom, is to approximate it by its spherically symmetric component, i.e.,

$$\langle \mathbf{q}'_3 | t^{(s)} | \mathbf{q}_3 \rangle \approx t_{00}(q_3, \mathbf{p}_3, \mathbf{q}) Y_{00}(\hat{\mathbf{q}}_3) = (4\pi)^{-1/2} t_{00}(q_3, \mathbf{p}_3, \mathbf{q}). \quad (20)$$

Equation (20) has the same structure as the peaking approximation, which evaluates the two-body t matrix setting $\mathbf{q}_3 = -\alpha\mathbf{q}/2$, i.e., using only the first term on the right-hand side of Eq. (19). Use of Eq. (19), however, gives results which, unlike the results obtained by using the peaking approximation,¹⁷ are time reversal invariant.¹³ This approach is called the part-classical approximation, previously called semiclassical (a new name is given to avoid confusion with other usage of the term semiclassical in scattering theory¹⁰), because it has one foot in classical mechanics. Equation (20) has been extensively used by us for calculating differential cross sections and has provided answers always within 10% of those given by a spot check of the exact calculation.^{4,18}

Recalling that $\phi(\mathbf{q}_3)$ is the wave function of the initial state in the momentum representation, i.e.,

$$\phi(\mathbf{q}_3) = \left(\frac{2}{\pi}\right)^{1/2} i^l I_{v,j}(\mathbf{q}_3) Y_{j,m}(\hat{\mathbf{q}}_3), \quad (21)$$

where v, j, m are the initial vibrational, rotational, and magnetic quantum numbers, respectively, and,

$$I_{v,j}(\mathbf{q}_3) = \int_0^\infty dy_3 y_3^2 \chi_{v,j}(y_3) j_l(q_3 y_3), \quad (22)$$

where $\chi_{v,j}$ is the vibration-rotation wave function in the coordinate space, we can integrate Eq. (18) over \mathbf{q}_3 . Using the Raleigh expansion of the plane wave, i.e.,

$$\exp(-i\mathbf{q}_3 \cdot \mathbf{y}_3) = 4\pi \sum_{l,m} (-i)^l Y_{lm}(\hat{\mathbf{y}}_3) Y_{lm}^*(\hat{\mathbf{q}}_3) j_l(q_3 y_3), \quad (23)$$

we obtain

$$\Psi^{(s)}(\mathbf{y}_3, \mathbf{q}, \mathbf{p}_3) = (4\pi)^{-1/2} K_{v,j}^{(s)}(\mathbf{y}_3, \mathbf{q}, \mathbf{p}_3) Y_{j,m}(\hat{\mathbf{y}}_3) \quad (24)$$

where

$$K_{v,j}^{(s)}(\mathbf{y}_3, \mathbf{p}_3, \mathbf{q}) = \frac{2}{\pi} \int_0^\infty dq_3 q_3^2 j_l(q_3 y_3) t_{00}^{(s)}(q_3, \mathbf{p}_3, \mathbf{q}) I_{v,j}(\mathbf{q}_3). \quad (25)$$

A comparison of Eqs. (24) and (25) with Eqs. (21) and (22) shows the similarity of their structure and provides further basis for the statement that $\Psi^{(s)}$ is the modified wave function for the internal motion of the diatom. Substituting Eqs. (18) through (25) into Eq. (17), we get

$$\begin{aligned} \langle \phi'_3 | T^{(s)}(\mathbf{q}) | \phi_3 \rangle &= \left(\frac{1}{4\pi}\right)^{1/2} \int dy_3 \phi'_3(y_3) Y_{j,m}(\hat{\mathbf{y}}_3) \\ &\times \exp(-i\alpha_s \mathbf{q} \cdot \mathbf{y}_3) K_{v,j}^{(s)}(\mathbf{q}, \mathbf{p}_3, y_3). \end{aligned} \quad (26)$$

Again using the Raleigh expansion of the plane wave and writing $\phi'_3(y_3) = \chi_{v',j'}(y_3) Y_{j',m'}(\hat{\mathbf{y}}_3)$, where primes denote the vibrational and rotational levels v', j' of the final state, we get

$$\begin{aligned} \langle \phi'_3 | T^{(s)}(\mathbf{q}) | \phi_3 \rangle &= \sum_l (\pm i)^l \left(\frac{[l][j]}{[j']}\right)^{1/2} N_{vjl'v'j'}^{(s)}(\mathbf{q}, \mathbf{p}_3) \\ &\times C(jl'j'; m, m' - m) \\ &\times C(jl'j'; 00) Y_{l, m' - m}^*(\hat{\mathbf{q}}), \end{aligned} \quad (27)$$

where C 's are the Clebsch-Gordan coefficients, $[j] \equiv (2j+1)$, and

$$\begin{aligned} N_{vjl'v'j'}^{(s)}(\mathbf{p}_3, \mathbf{q}) &= \int_0^\infty dy_3 y_3^2 \chi_{v',j'}(y_3) j_l(\alpha_s |q y_3) \\ &\times K_{v,j}^{(s)}(\mathbf{p}_3, \mathbf{q}, y_3). \end{aligned} \quad (28)$$

Taking our space fixed z axis along \mathbf{q} , and using the relation

$$Y_{l,m}^*(0,0) = \left(\frac{[l]}{4\pi}\right)^{1/2} \delta_{m,0} \quad (29)$$

we get

$$\begin{aligned} \langle \phi'_3 | T^{(s)}(\mathbf{q}) | \phi_3 \rangle &= (4\pi)^{-1/2} \sum_l (\pm i)^l \left(\frac{[l]}{[j']}\right)^{1/2} \\ &\times [l] N_{vjl'v'j'}^{(s)}(\mathbf{q}, \mathbf{p}_3) C(jl'j'; m, 0) \\ &\times C(jl'j'; 00). \end{aligned} \quad (30)$$

Using the relation¹⁹

$$\sum_m C(jl'j'; m, 0) C(jl'j'; m, 0) = \left(\frac{[j']}{[l]}\right)^{1/2} \delta_{l,j'}, \quad (31)$$

we can write, using Eqs. (13) and (16)

$$\begin{aligned} \frac{d\sigma}{d\Omega}(i \equiv v j p_3 \rightarrow f \equiv v' j' p'_3; \mathbf{q}) \\ = \frac{p'_3}{p_3} (2j+1)^{-1} \mu_3^2 \left(\frac{2\pi}{\hbar}\right)^4 \left(\frac{1}{4\pi}\right)^4 \sum_{l=j'-j}^{j'+j} [l] C^2(jl'j'; 00) \\ \times \left| N_{vjl'v'j'}^{(1)} + (-)^l N_{vjl'v'j'}^{(2)} \right|^2. \end{aligned} \quad (32)$$

Equation (32) is our final result and is obtained by adding the amplitudes for scattering from the two scattering centers.

IV. COMPUTATIONS

In this section we briefly describe the computational procedures followed. These procedures are the same as in the previous work on the collision of alkali halide molecules with argon.^{4,18} Briefly, since the ground state of CsF is ionic, the Ar-CsF potential is taken to be the sum of Ar-Cs⁺ and Ar-F⁻ potentials. Only the repulsive portion of the Ar-ion potential, which is approximated by a hard core potential, is used in the present calculations. The hard core radii for the Ar-Cs⁺ and Ar-F⁻ potentials are assumed to be given by the corresponding parameters for the Ar-Xe and Ar-Ne potentials.²⁰ The parameters for the diatom potential are taken from Huber and Herzberg.²¹ The potential function thus obtained is extrapolated to larger internuclear distances using a Padé [2,2] approximant. Wave functions for the internal motion of the diatom are obtained by solving the one dimensional Schrödinger equation, containing the centrifugal term for the rotational motion, using Numerov's method.

V. MECHANISMS GIVING RISE TO THE BALLISTIC PEAK

Before we compare the calculated differential cross sections with the experimental values, it is desirable that we discuss the physical basis for the ballistic peak. Figure 1, plotted using the points taken from the earlier work,² gives a plot of the laboratory differential cross section as a function of CsF recoil velocity and illustrates the experimental data we are trying to model. The ballistic peak on the left, near the centroid velocity, represents the signal from those molecules that have small c.m. recoil velocities and which carry large amounts of internal excitation.¹ The ballistic peak was shown⁴ to arise when Ar strikes the F end of CsF.

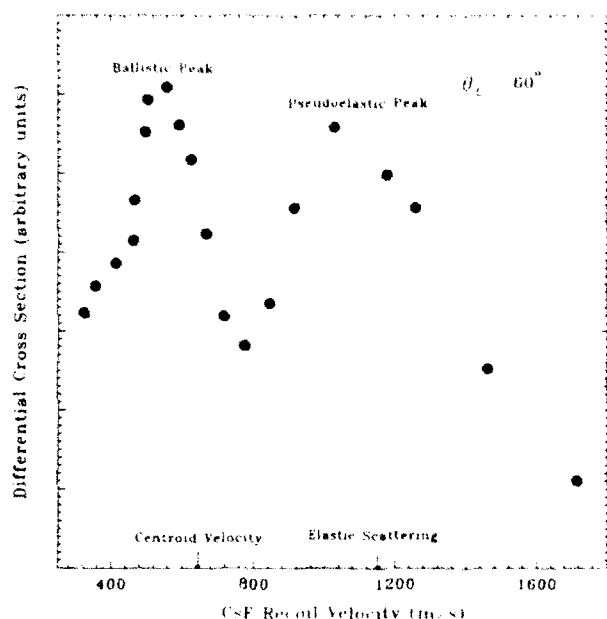


FIG. 1. Laboratory differential cross section as a function of the laboratory recoil velocity of CsF at the laboratory scattering angle of 60° . This figure is reproduced from Ref. 3. The pseudoelastic peak, centered at the recoil velocity of about 1100 m/s, is where elastic scattering at large c.m. scattering angles (about 150°) should be observed. The peak at about 500 m/s is the ballistic peak and is centered near the centroid velocity. The CsF molecules contributing to this peak are moving slowly in the c.m. frame.

The peak on the right, called the pseudoelastic peak,⁴ centered at the recoil velocity corresponding to elastic scattering, arises⁴ when Ar strikes the Cs end of CsF and consists of inelastic transitions involving modest changes ($|\Delta E|/E < 0.35$) of collision energy. An earlier model of impulsive atom-diatom collisions predicts⁵ a transfer of only 14% of the initial relative translational energy into internal energy, i.e., ($|\Delta E|/E \approx 0.14$), when Ar hits the Cs end of CsF. The results of our calculation and those of the earlier model are in disagreement. Comparison of our calculation with the experimentally observed pseudoelastic peak will decide if our theory is correct.

It was shown earlier⁴ that when one is looking along or close to the direction of the centroid velocity, most of the contribution to the ballistic peak comes from the transitions which convert more than 97% of the relative translational energy into internal energy. Further, the signal from a transition which converts more than 99% of the relative translational energy into internal motion (resonant transition) may be larger than the signal from any other transition by a factor of about 2-3. It was also pointed out that the c.m. differential cross section for the resonant transitions is within a few percent of the neighboring non-resonant transitions. What sets the resonant transitions apart from the nearby transitions is the large Jacobian of transformation from the c.m. to the laboratory coordinate system, which is very sensitive to the fraction of relative translational energy converted into internal energy. The expression for the Jacobian is derived in the Appendix. Figure 2 is a plot of the Jacobian for the transformation

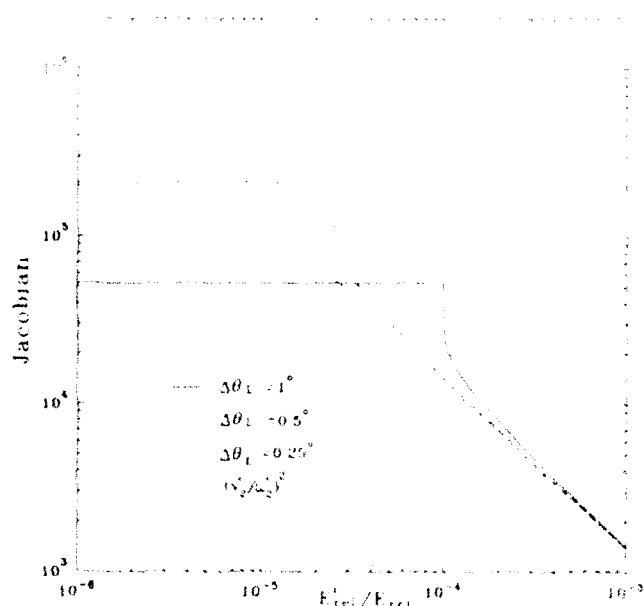


FIG. 2. Jacobian for the transformation of the differential cross section from the c.m. frame to the laboratory frame as a function of the final relative translational energy of CsF (measured as a fraction of the initial relative translational energy) when the scattering is viewed along the direction of the centroid velocity, i.e., $\theta_2 = \theta_L$.

from the c.m. to the laboratory coordinates, for the laboratory scattering angle equal to the angle of the centroid velocity, as a function of the fraction of the relative translational energy converted into internal energy. It is readily seen from this figure why the differential cross section for the resonant transitions in the laboratory frame is so much larger than the neighboring transitions.

When the recoil velocities of the alkali halide molecules in the c.m. frame and the laboratory frame are perpendicular, the laboratory scattering angle for two values, a maximum and a minimum, displays an extremum as a function of the c.m. scattering angle. The laboratory scattering cross section, for these two values of laboratory scattering angles, exhibits a rainbowlike singularity. Figure 3 gives a plot of the differential cross section, obtained by summing over the two branches in Fig. 16, in the laboratory (c.m.) frame as a function of laboratory (c.m.) scattering angle. The collision parameters are given in Fig. 15. The minimum (maximum) laboratory scattering angle of 30° (75°) correspond to c.m. scattering angles of 18° (117°). An order of magnitude enhancement of the differential cross section due to the kinematic rainbowlike singularity (edge effect) is seen. The values of the minimum and maximum laboratory angles are dependent upon the transition under consideration. These kinematic rainbows, called the edge effect,¹¹ are the cause of the ballistic peak when the laboratory scattering angle is much different from the direction of the centroid velocity.

VI. COMPARISON OF THE CALCULATION WITH THE EXPERIMENTAL RESULTS

The calculated results are compared with the experimental results after they are scanned over by a normalized

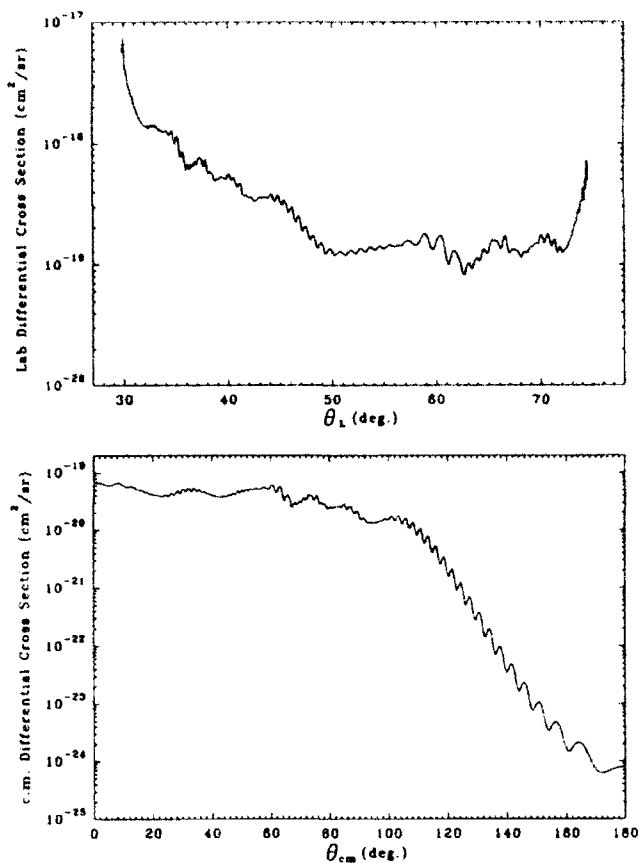


FIG. 3. Calculated laboratory (c.m.) differential cross section (cm^2/sr) as a function of laboratory (c.m.) scattering angle. Increased differential cross section at the minimum and maximum laboratory scattering angles is due to the kinematic rainbows, also called edge effect (Ref. 11), and not due to any peculiarities in the c.m. differential cross section. The collision parameters are the same as in Fig. 15.

Gaussian function with the resolution ratio¹ $R \equiv (\Delta v_1/v_1) = (19.3 + 0.034v_1)$, where R is expressed in percent, Δv_1 is the full-width at half-maximum of the Gaussian, and v_1 is in units of m/s. To understand the role of the resolution ratio in the experimental results, we plot in Fig. 4 the output signal (dashed line) in arbitrary units as a function of the velocity of Ar when the input (solid line) is given by $P(v_1) = v_1^3 \exp(-[(v_1 - \langle v_1 \rangle)/\delta v_1]^2)$ with $\langle v_1 \rangle = 2380$ m/s and $\delta v_1 = 350$ m/s. It is seen that while the input velocity peaks at 2450 m/s (1.0 eV translational energy),²² the output velocity peaks at about 2050 m/s. This shift due to the velocity dependent resolution function leads to the actual energy being about 50% larger than the nominal energy. Because the resolution function severely distorts the calculated results, we will, after comparing the calculated results with the experimental measurements and establishing their credibility, present the undistorted calculated results. This will permit us to examine the calculation more closely and to see if any other lessons can be learned from it.

To determine the dependence of the calculated results on the initial translational velocity of Ar, we plot in Fig. 5 the laboratory differential scattering cross section as a

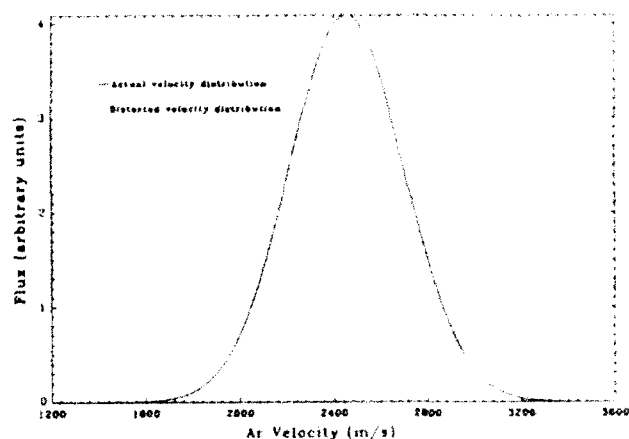


FIG. 4. Flux of the Ar parent beam, in arbitrary units, as a function of the velocity of Ar. The input function (solid line) represents the actual velocity distribution and is given by $P(v_1) = v_1^3 \exp(-[(v_1 - \langle v_1 \rangle)/\delta v_1]^2)$ with $\langle v_1 \rangle = 2380$ m/s and $\delta v_1 = 350$ m/s. The output velocity distribution (dotted line), represents the measured Ar parent beam flux and is obtained by modifying the input distribution by a normalized Gaussian function with full-width at half-height given by the resolution function R . The actual velocity distribution peaks at 2450 m/s, but the measured peak is at about 2050 m/s. The energy associated with the output distribution peak is about 71% of the energy corresponding to the maximum of the input distribution.

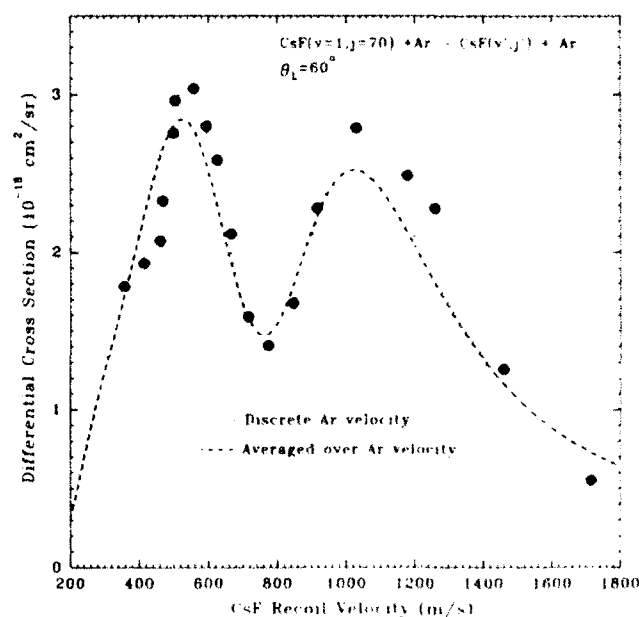


FIG. 5. Laboratory differential cross section as a function of the laboratory recoil velocity of CsF at the laboratory scattering angle of 60° . Dotted line is the result of the impulse calculation for Ar velocity $v_1 = 2450$ m/s and CsF velocity $v_2 = 500$ m/s with the initial state of CsF given by $v = 1$ and $j = 70$. The dashed line is the result of the impulse calculation obtained by averaging over the Ar velocity according to the distribution given in Ref. 1; the velocity of the CsF beam is still 500 m/s. The experimental points are the same as in Fig. 1, taken from Ref. 3, and are normalized to match the calculation for discrete velocity at the largest cross section.

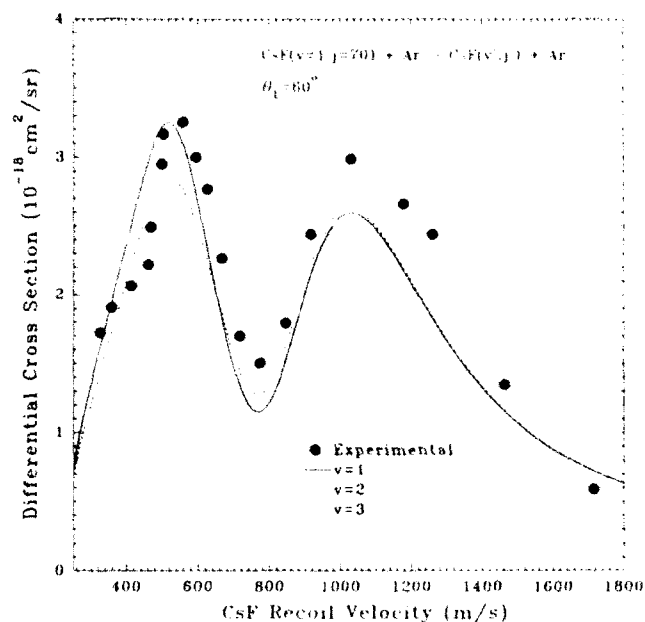


FIG. 6. Laboratory differential cross section as a function of the laboratory recoil velocity of CsF at the laboratory scattering angle of 60° . The velocity of the Ar and the CsF beams are $v_1 = 2450$ m/s and $v_2 = 500$ m/s with the initial rotational state of CsF fixed at $j = 60$. The impulse calculations for initial vibrational levels $v = 1, 2$, and 3 are represented by solid, dotted, and dashed lines, respectively.

function of the laboratory recoil velocity of CsF at the laboratory scattering angle of 60° . The dotted line is our impulse calculation for the Ar velocity $v_1 = 2450$ m/s and the CsF velocity $v_2 = 500$ m/s with the initial state of CsF given by $v = 1$ and $j = 70$. The dashed line is the impulse calculation using the probability of the Ar velocity given by the formula $P(v_1) = v_1^3 \exp(-[(v_1 - \langle v_1 \rangle)/\delta v_1]^2)$, while keeping the CsF velocity at 500 m/s. The experimental points are the same as in Fig. 1, taken from Ref. 3, and are normalized to match the calculation at the largest cross section. It is seen that the calculation is insensitive to averaging over the initial velocity distribution of Ar. Since most of the initial translational energy is supplied by Ar, it appears reasonable to assume that the calculation is also insensitive to averaging over the initial CsF velocity distribution. In the rest of the paper we will present the calculations for fixed velocities of the Ar and the CsF beams.

To investigate the variation of the calculated results with the initial vibrational quantum number of CsF, we plot in Fig. 6 the laboratory differential scattering cross section as a function of the laboratory recoil velocity of CsF at the laboratory scattering angle of 60° . The velocity of the Ar beam is fixed at $v_1 = 2450$ m/s, while that of the CsF beam is fixed at $v_2 = 550$ m/s. The initial rotational level of CsF is fixed at $j = 60$. Solid curve, dotted, and dashed curves are the results of our calculation for initial vibrational levels $v = 1, 2$, and 3 , respectively. The experimental points are the same as in Fig. 1, taken from Ref. 3, and are normalized to match the calculation at the largest cross section. It is seen that the calculation is insensitive to the initial vibrational level of CsF. In the remainder of the

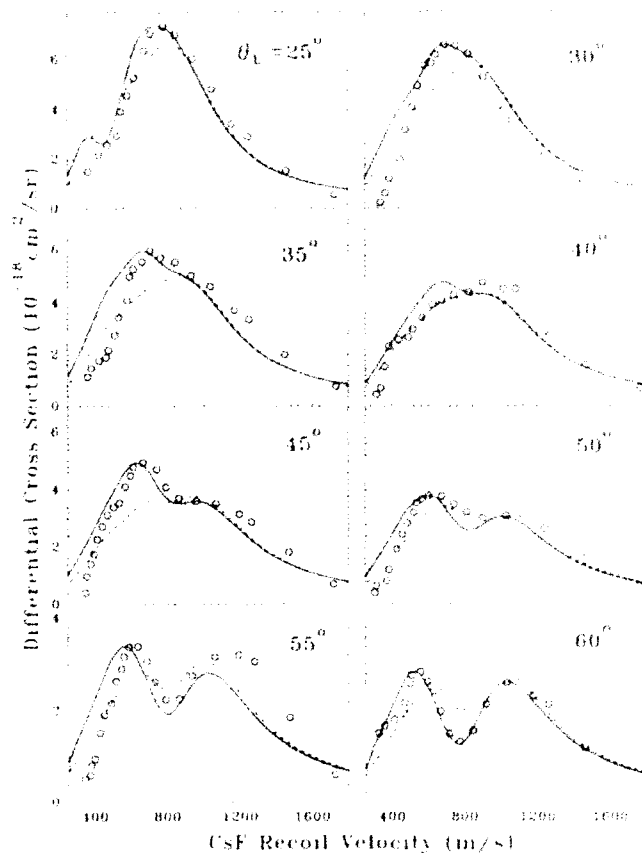


FIG. 7. Laboratory differential cross section as a function of the laboratory recoil velocity of CsF at eight laboratory scattering angles 25° – 60° . The velocity of the Ar and the CsF beams are $v_1 = 2450$ m/s and $v_2 = 500$ m/s with the initial vibrational state of CsF fixed at $v = 3$. The impulse calculations for initial rotational levels $j = 60, 100$, and 30 are represented by solid, broken, and dotted lines, respectively.

paper we will assume that initial vibrational level of CsF is $v = 3$ because this is the average vibrational level at 1000 K, the temperature of the CsF beam.

To investigate the dependence of the calculated differential cross sections on the initial rotational quantum number of CsF and to compare the calculated results with the experimentally measured ones, we plot in Fig. 7 the laboratory differential scattering cross section as a function of the laboratory recoil velocity of CsF at eight laboratory scattering angles: $25^\circ, 30^\circ, \dots, 60^\circ$. The velocity of the Ar beam is fixed at $v_1 = 2450$ m/s; while that of the CsF beam is fixed at $v_2 = 500$ m/s. The initial vibrational level of CsF is fixed at $v = 3$. Dotted, solid, and dashed curves correspond to CsF initial rotational levels $j = 30, 60$, and 100 , respectively. The experimental points are taken from Ref. 3, and are normalized at each angle separately, to match the calculation for $j = 60$ at the largest cross section. It is seen that the calculation is sensitive to the initial rotational level of CsF, and the best agreement for all eight laboratory scattering angles is given by the solid line, i.e., $j = 60$.

The calculated results are in excellent agreement with the measured ones at all of the eight available laboratory scattering angles. The calculated results are not very sen-

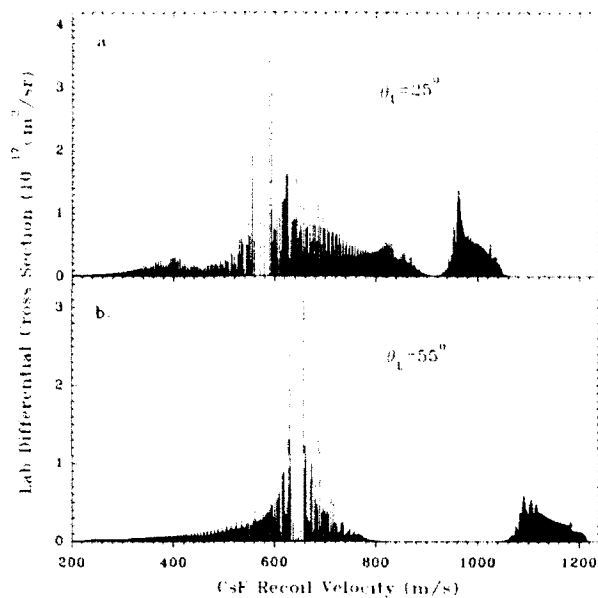


FIG. 8. Calculated laboratory differential cross section as a function of the laboratory recoil velocity of CsF for the laboratory scattering angles of 25° and 55° for initial vibrational-rotational level ($v=3, j=60$) of CsF. The remainder of the beam parameters are the same as in Fig. 7.

sitive to the initial velocity distribution of the Ar beam or to the initial vibrational quantum number of the CsF beam. They are, however, sensitive to the initial rotational distribution of the CsF beam. The calculated results imply that the rotational distribution of the CsF beam peaks around $j=60$, rather than $j=30$ or $j=100$. In other words, the rotational temperature of the beam, if our calculation is to be believed, is close to 1000 K, the temperature of the oven.

A word of caution here is, perhaps, in order. We are not saying that the magnitude of the ballistic peak in CsF-Ar system is independent of the initial relative translational energy, but that it is insensitive to whether one performs the calculation at the average initial relative translational energy of 1.0 eV or averages the calculated differential cross sections over the experimental¹ Maxwell distribution centered at 1.0 eV. The magnitude of the ballistic peak does depend upon the initial relative velocity as is shown by the fact that our model predicts a ballistic peak for the I_2 -Ar (I_2 beam temperature 250 K) at the initial relative translational energy of 0.12 eV, but not at 1.0 eV. Similarly, it is being stated that the magnitude of the ballistic peak is independent of the initial vibrational level of CsF only if that vibrational level is one of the first four levels.

VII. DETAILED EXAMINATION OF THE CALCULATED RESULTS

Because the resolution of the instrument distorts the calculated signal so severely, we present, in Fig. 8, the calculated discrete spectra for 55° and 25° laboratory scattering angles. The initial rotational level of CsF for these calculations is $j=60$; the remaining beam parameters are the same as in Fig. 7, and the angle of the centroid velocity

vector in the laboratory frame is 52.2°. The contribution to the ballistic peak at the laboratory scattering angle of 55° is dominated by the resonant transfer of the relative translational energy into the internal motion, while at the laboratory scattering angle of 25°, it is determined by the kinematic rainbow, or the edge effect.¹¹ This is also the conclusion arrived at from Fig. 8 where, for the 55° scattering the ballistic peak is centered at the recoil velocity equal to the velocity of the c.m., while for the 25° scattering the center of the ballistic peak is at a lower value of recoil velocity. The ballistic peak for the laboratory scattering of 55° is centered at the c.m. velocity of 646 m/s, because when all of the energy of relative translational motion has been resonantly transferred into internal energy, the molecule is stationary in the c.m. frame and it moves at the velocity of the c.m. in the laboratory frame. The molecules contributing to the ballistic peak at the 25° scattering angle have a substantial c.m. recoil velocity, and here the ballistic peak arises because of the kinematic rainbow, or edge effect.¹¹ For this case the recoil velocity of the molecule in the laboratory frame is perpendicular to its recoil velocity in the laboratory frame, leading to the relationship $(v_2')^2 = (v_{c.m.})^2 - (\omega_2')^2$. The laboratory recoil velocity, around which the ballistic peak is centered, is now smaller (about 575 m/s) than the velocity of the c.m.

It is worth noting that the ballistic peak for the 55° laboratory scattering angle displays a profile similar to a Lorentzian. This is because the c.m. differential cross sections for the dominant transitions are, because of the density factor, proportional to the c.m. recoil velocity. The Jacobian varies inversely as the square of the c.m. recoil velocity. The laboratory differential cross sections are therefore inversely proportional to the c.m. recoil velocity (the Lorentzian profile would be inversely proportional to the square of the c.m. recoil velocity).

The ballistic peak at the 25° scattering angle has a more complicated structure than that at 55°. There are more transitions comprising the 25° peak that have noticeably large cross section. In addition, the transitions are not symmetrically placed around the central recoil velocity of 575 m/s. These observations can be understood by referring to Fig. 9, which gives a plot of the absolute value of the Jacobian, for several laboratory scattering angles vs the laboratory recoil velocity of CsF for a 0.25° wide detector. When the laboratory scattering angle is equal to the laboratory angle of the centroid velocity (52.2°), the Jacobian is extremely large and very sharply peaked. As we move away from the direction of the centroid velocity, i.e., increase or decrease the laboratory scattering angle, the value of the Jacobian becomes smaller, the peak gets flatter, and the center of the peak moves towards smaller recoil velocities. This is because the farther we look from the direction of the c.m. velocity, the larger ω_2' must be, and therefore the smaller v_2' must be so that the square of these two recoil velocities can be equal to the square of the centroid velocity. Because the Jacobian is much flatter at the 25° scattering angle, the laboratory differential cross sections resemble the c.m. differential cross sections. These points are apparent in Fig. 10, which gives a plot of the

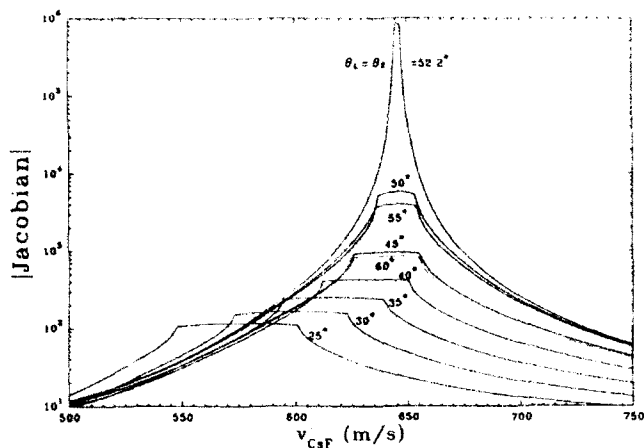


FIG. 9. Absolute value of the Jacobian for the transformation of the differential cross section from the c.m. coordinate system to the laboratory coordinate system as a function of the laboratory recoil velocity of CsF for various laboratory scattering angles.

c.m. differential cross section as a function of the laboratory recoil velocity of CsF at the laboratory scattering angles of 25° and 50°. Since we are assuming an idealized beam without lateral dimensions, each stick in the figure corresponds to a c.m. differential cross section at a definite c.m. scattering angle. Therefore, the c.m. differential cross sections in Fig. 10, upon multiplication with the appropriate Jacobian (Fig. 9) given the laboratory differential cross sections, plotted in Fig. 8. The c.m. differential cross sections resemble the laboratory differential cross sections for the 25° scattering angle; for the 55° scattering angle, on the other hand, the transitions most prominent in the labora-

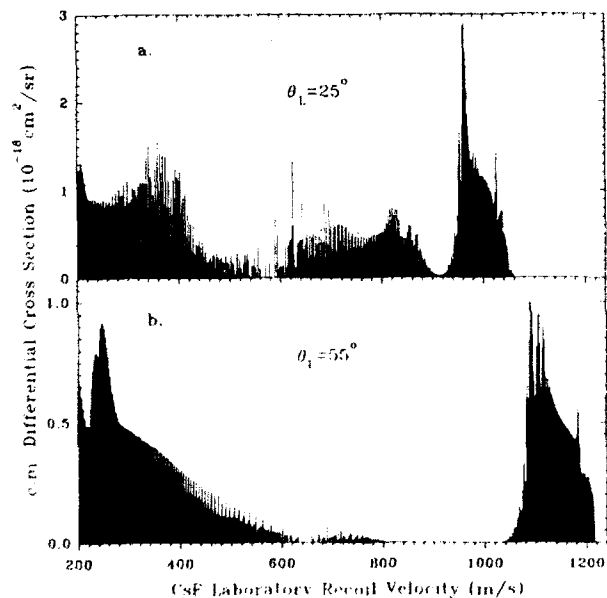


FIG. 10. Center-of-mass differential cross section (cm^2/sr) as a function of the laboratory recoil velocity (m/s) of CsF at the laboratory scattering angles of 25° (top frame) and 55° (bottom frame). The beam parameters are the same as in Fig. 8.

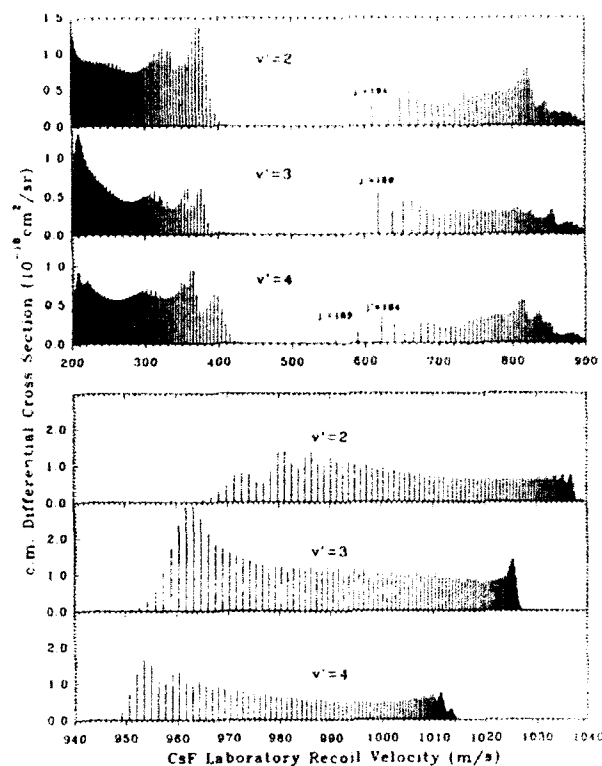


FIG. 11. Center-of-mass differential cross section (cm^2/sr) as a function of the laboratory recoil velocity (m/s) of CsF at the laboratory scattering angle of 25°, for the most prominent transitions making up the ballistic peak (top three frames), and the most prominent transitions making up the pseudoelastic peak (bottom three frames). The beam parameters are the same as in Fig. 8.

tory frame (Fig. 8) are barely noticeable in the c.m. frame. It should also be noticed that the pseudoelastic peak shifts to smaller recoil velocities as the laboratory scattering angle moves away from the direction of the centroid velocity; the maximum intensity occurs at the recoil velocity of 960 m/s for 25° and at 1100 m/s for 55°. This happens because, when the laboratory scattering angle is farther from the direction of the centroid velocity the angle between ω'_2 and $v_{\text{c.m.}}$ becomes closer to 90°, resulting in smaller value of $v'_2 = [(\omega'_2)^2 + (v_{\text{c.m.}})^2 - 2\omega'_2 \cdot v_{\text{c.m.}}]^{1/2}$.

A closer look at the details of the scattering at 25° is provided by Fig. 11, which is a plot, again for an idealized beam, of the c.m. differential cross section as a function of the laboratory recoil velocity of CsF. The initial state of CsF is $v=3$, $j=60$; the Ar-CsF initial relative translational energy is 1.0 eV; the c.m. velocity is 646 m/s at a laboratory angle of 52.5°. The three upper frames are the rotational transitions comprising the ballistic peak (Ar-F encounter) for final vibrational levels $v'=2, 3$, and 4; the three lower frames are the rotational transitions comprising the pseudoelastic peak (Ar-Cs encounter) for the same final vibrational levels. The rotational transitions comprising the ballistic peak have almost the same structure and appear to be independent of the final vibrational level. Be-

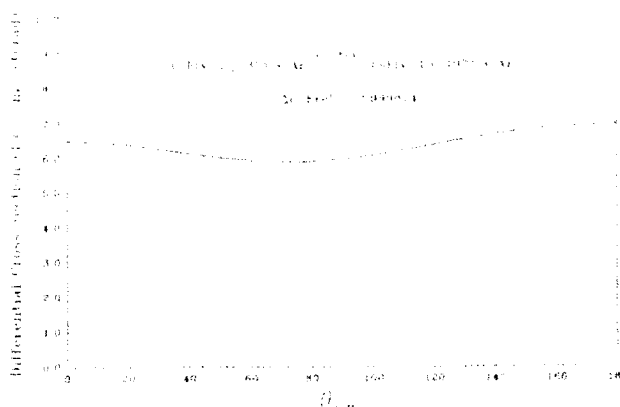


FIG. 12. Calculated c.m. differential cross section as a function of the c.m. scattering angle. When almost all of the initial relative translational energy has been converted into internal motion, the final relative translational energy carries no angular momentum, leading to isotropic scattering.

tween the recoil velocities of 200 and 400 m/s there are supernumerary rainbows and a primary rainbow in each frame, and a secondary rainbow in the $v'=4$ frame, the rotational quantum number increasing with increasing recoil velocity. On the right side of each frame, after a larger gap in the center, the rotational quantum number decreases with increasing recoil velocity and the transitions appearing first, i.e., closest to 575 m/s recoil velocity, are constrained by the kinematic rainbowlike singularity or the edge effect. The rotational transitions $j'=194$, 189, and 185 are the first to appear for the final vibrational quantum numbers 2, 3, and 4, respectively. The highest final rotational level attainable is greater for smaller vibrational quantum numbers because more energy is available when the final vibrational quantum number is smaller. One can regard these rotational transitions as dynamical rainbows and state that kinematic rainbows lead to dynamic rainbows. As the recoil velocity increases and the final rotational quantum number decreases, the supernumerary, primary, and secondary rainbows are again seen. The differential cross sections comprising the ballistic peak exhibit a rich and complicated structure.

For the case of pseudoelastic scattering (Ar-Cs encounter) depicted in the lower three frames of Fig. 11, there are at least two rotational rainbows in each frame. The frame corresponding to $v'=2$ exhibits a secondary rainbow on the left, while that for $v'=4$ exhibits a secondary rainbow on the right. The smaller recoil velocities correspond to larger final rotational quantum numbers, while the larger recoil velocities correspond to smaller final rotational quantum numbers. The inelastic transitions move towards larger recoil velocities as more energy becomes available, i.e., as the final vibrational quantum number decreases. The limit of the change in the rotational quantum number is dictated by the conservation of angular momentum.

Figure 12 is a plot of the c.m. differential cross section as a function of the c.m. scattering angle. It is seen that

when almost all of the initial relative translational energy has been converted into the internal energy, the c.m. differential cross section is independent of the c.m. scattering angle. This effect, which was predicted earlier,⁴ arises because, for the resonant energy transfer from translation to vibration-rotation, the final orbital motion has very small relative velocity and is therefore an isotropic s wave. This is one of the rare instances in atom-diatoms collisions when one encounters partial waves with very low quantum numbers.

VIII. CONCLUSIONS

The basic question is, why do the experimental results agree with the calculated results, which are obtained by using a simplified atom-diatom potential? Not only has the atom-diatom potential been approximated by the sum of two atom-atom potentials, the atom-atom potentials have in addition to this approximation been replaced by two hard core potentials. A clue to the answer is provided by earlier work¹⁸ which studied the deactivation of highly vibrationally excited KBr by Ar using exactly the same calculation. For the largest c.m. scattering angle (75°) for which the experimental measurements were available, the calculated c.m. differential cross section plotted as a function of the KBr c.m. recoil velocity agreed with the experimental measurements for all recoil velocities (0–1000 m/s). For the smallest c.m. scattering angle (45°) for which the experimental measurements were available, on the other hand, the calculated c.m. differential cross section plotted as a function of the KBr c.m. recoil velocity agreed with the experimental measurements only for recoil velocities larger than about 700 m/s. The answer, then, lies in noting that (i) the pseudoelastic peak, involving transfers of small amounts of energy between translation and rotation-vibration, corresponds to large c.m. scattering angles for which the attractive portion of the potential, in analogy with the KBr-Ar results, makes no contribution, (ii) the ballistic peak involves transfer of a large fraction of the initial relative translational energy into internal energy, which can be caused, again in analogy with the KBr-Ar results, only by the repulsive portion of the potential independent of the c.m. scattering angle and, (iii) the calculation is insensitive to the steepness of the repulsive portion of the potential. Preliminary work²¹ with the exponential repulsive potential supports this conclusion. We have a situation where the two ends of the diatom scatter, independent of each other, from the repulsive part of the atom-atom interaction potential. Further, the scattering from the repulsive portion of the potential does not appear to strongly depend upon the steepness of the repulsive potential. This, we believe, is why this calculation works so well.

It was pointed out earlier that the Jacobian for the transformation from the c.m. to the laboratory frame may lead to the enhancement of the c.m. differential cross section by a factor of a million. This result is derived assuming an idealized beam of infinitesimal extent. For a beam with finite width and a detector of finite dimensions, the ballistic peak along the direction of the c.m. velocity will contain contributions from transitions which are not exactly reso-

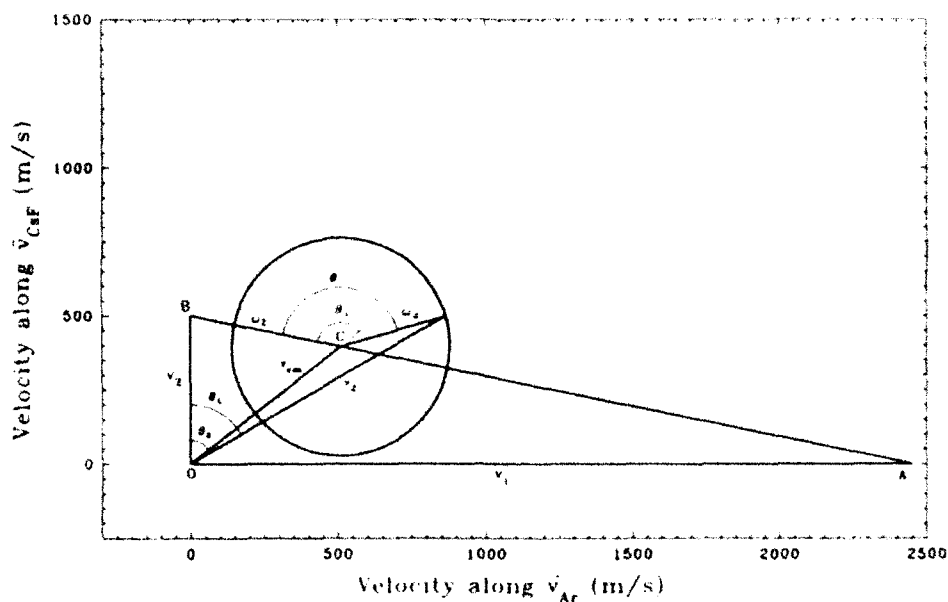


FIG. 13. Vector diagram for the CsF-Ar scattering. The initial laboratory velocity of the Ar beam (v_1) is measured along the X axis and that of the CsF (v_2) beam along the Z axis. The laboratory angles are measured from the direction of the CsF beam; θ_1 and θ_L are the laboratory angles of the centroid velocity v_{cm} and the recoil velocity v_r^* (laboratory scattering angle), respectively. The c.m. scattering angle is measured from CB, the direction of initial c.m. velocity of CsF (ω_2). The pseudoelastic peak discussed in this article, centered at a laboratory recoil velocity of about 1000 m/s, arises from the larger c.m. scattering angles. The other pseudoelastic peak, centered at a laboratory recoil velocity of about 150 m/s, arising from smaller c.m. scattering angles, was not experimentally detected and will not be further discussed. The circle in the figure corresponds to one-half of the initial relative translational energy being converted into internal energy.

nant $T \rightarrow (V,R)$ processes. This may lead to an average value of the Jacobian which is considerably less than a million. The actual value will depend not only upon the extent of the two beams and the spread of their velocities, but also upon the molecule being studied. If the molecule has a large rotational constant and the energy spread of the beams is smaller than the spacing between the final rotational levels, the average Jacobian may still be close to a million. The parameters of the beams, the molecule studied, and the dimensions of the detector will all have to be carefully considered for a more detailed answer.

Our results require that the CsF beam in the experiments¹⁻³ must not be rotationally relaxed. In fact, the observation of a ballistic peak for the CsI-Ar system and the nonobservation of one for the I₂-Ar system at the same relative translational energy (≈ 1 eV) is explained by our model by postulating that transitions from higher rotational levels populated in the CsI beam (oven temperature ≈ 1000 K) lead to conversion of a much larger fraction of relative translational energy into internal energy than the low rotational levels available in the cooler (oven temperature ≈ 250 K) I₂ beam. This provides another test of our model.

Our calculations have been performed assuming idealized beams with infinitesimal extent. Still they agree remarkably well with experimental measurements. Perhaps it is because the broadening of the calculated results by the resolution function, discussed earlier, is much larger than that due to the finite extent of the colliding beams.

It is also useful to point out that, since our calculation agrees so well with the experimental results for both the

pseudoelastic peak and the ballistic peak, the earlier model of impulsive collisions,⁵ which certainly gives a much different value for the energy transferred during both the pseudoelastic and the ballistic collisions, may need to be re-examined.

Perhaps the most important results of this study is that the ballistic effect should be observable for all collision systems under appropriate circumstances.

This work was in part funded by AFOSR under task 2303EP and Phillips Laboratory project 007. The authors are grateful to Dudley Herschbach for many interesting discussions and making available to them the relevant portions of the Ph.D. theses of Dr. Entemann, Dr. King, and Dr. Zare.

APPENDIX

To derive the expression for the Jacobian of transformation between the laboratory and the center of mass coordinates as shown in Fig. 13, we pick the following notation:

- (i) v_1 , the initial velocity of Ar atoms, is along the X axis in the laboratory coordinate system;
- (ii) v_2 , the initial velocity of the alkali halide, is along the Z axis in the laboratory coordinate system;
- (iii) the coordinate system fixed in the laboratory frame is denoted by XYZ while that fixed in the c.m. frame is denoted by xyz .

The initial relative velocity and the velocity of the c.m. are, obviously, in the XZ plane in the laboratory coordi-

nate system. We also take this plane to be the xz plane of the c.m. coordinate system. In addition, we assume that the detector is also centered in this plane. θ_L and θ_2 are the polar angles of the alkali halide recoil velocity v_2' and of the centroid velocity $v_{c.m.}$, respectively, in the laboratory coordinate system. θ_1 is the angle between the initial velocity ω_2 of the alkali halide in the c.m. frame and the centroid velocity $v_{c.m.}$. θ (the scattering angle) is the angle between the c.m. initial (ω_2) and c.m. final (recoil, ω_2') velocities of the alkali halide and ϕ is the azimuthal angle of ω_2' , measured from the xz plane. It should be pointed out that while the differential solid angle in the laboratory fixed axis is $d\Omega_L = \sin \theta_L d\theta_L d\phi_L$, the element of solid angle in the c.m. frame is $d\Omega = \sin(\theta - \theta_1 + \theta_2) d\theta d\phi$. The vector equation

$$v_2' = v_{c.m.} + \omega_2' \quad (\text{A1})$$

can be rewritten as

$$\begin{aligned} \gamma_1 \cos \theta_L &= \gamma \cos \theta_2 + \cos(\theta - \theta_1 + \theta_2), \\ \gamma_1 \sin \theta_L \cos \phi_L &= \gamma \sin \theta_2 + \sin(\theta - \theta_1 + \theta_2) \cos \phi \end{aligned} \quad (\text{A2})$$

$$\gamma_1 \sin \theta_L \sin \phi_L = \sin(\theta - \theta_1 + \theta_2) \sin \phi,$$

where $\gamma \equiv v_{c.m.}/\omega_2'$ and $\gamma_1 \equiv v_2'/\omega_2'$. From Eqs. (A2) we get

$$\tan \phi_L = \frac{\sin \phi}{[\gamma \sin \theta_2 / \sin(\theta - \theta_1 + \theta_2) + \cos \phi]},$$

yielding

$$\sin \phi_L = \frac{\sin \phi}{\left(1 + \gamma^2 \frac{\sin^2 \theta_2}{\sin^2(\theta - \theta_1 + \theta_2)} + 2\gamma \frac{\sin \theta_2 \cos \phi}{\sin(\theta - \theta_1 + \theta_2)}\right)^{1/2}}.$$

Differentiating this equation, we get

$$\left| \frac{d\phi_L}{d\phi} \right| = \left| 1 + \frac{\gamma \sin \theta_2 \cos \phi}{\sin(\theta - \theta_1 + \theta_2)} \right| \quad (\text{A3})$$

We now recall that our detector is centered in the XZ plane. This enables us to put $\phi = 0$ in the above equation obtaining

$$\left| \frac{d\phi_L}{d\phi} \right|^{-1} = \left| 1 + \gamma \frac{\sin \theta_2}{\sin(\theta - \theta_1 + \theta_2)} \right| = \left| \frac{\gamma_1 \sin \theta_L}{\sin(\theta - \theta_1 + \theta_2)} \right| \quad (\text{A4})$$

To obtain the relation between $d\theta$ and $d\theta_L$, we rewrite Eqs. (A2) for $\phi = 0$,

$$\begin{aligned} \gamma_1 \cos \theta_L &= \gamma \cos \theta_2 + \cos(\theta - \theta_1 + \theta_2), \\ \gamma_1 \sin \theta_L &= \gamma \sin \theta_2 + \sin(\theta - \theta_1 + \theta_2). \end{aligned} \quad (\text{A5})$$

Squaring the above equations and adding gives

$$\gamma_1^2 = \gamma^2 + 1 + 2\gamma \cos(\theta - \theta_1). \quad (\text{A6})$$

Dividing the second equation (A5) by the first one, we get

$$\tan \theta_L = \frac{\gamma \sin \theta_2 + \sin(\theta - \theta_1 + \theta_2)}{\gamma \cos \theta_2 + \cos(\theta - \theta_1 + \theta_2)},$$

resulting in

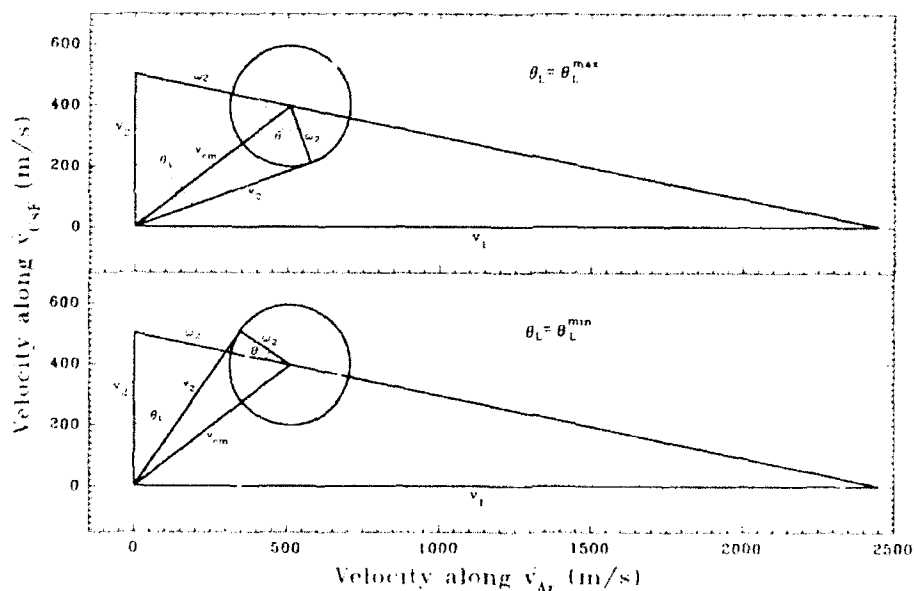


FIG. 14. Vector diagrams to demonstrate the existence of maximum (top figure) and minimum (bottom figure) laboratory scattering angles for a given value of the c.m. recoil velocity (ω_2') of CsF. At the maximum and minimum laboratory scattering angles, the c.m. and laboratory recoil velocities are perpendicular. The extrema in the laboratory scattering angle, as a function of the c.m. scattering angle, lead to rainbowlike singularities in the Jacobian for the c.m. to laboratory transformation at these points.

$$\cos \theta_L = \frac{\gamma \cos \theta_2 + \cos(\theta - \theta_1 + \theta_2)}{[1 + \gamma^2 + 2\gamma \cos(\theta - \theta_1)]^{1/2}} \quad (\text{A7})$$

Differentiating,

$$\begin{aligned} \left| \frac{d\theta_L}{d\theta} \right|^{-1} &= |\sin \theta_L| [1 + \gamma^2 + 2\gamma \cos(\theta - \theta_1)]^{3/2} \\ &\quad \times \{ \gamma^2 \cos(\theta - \theta_1) \sin \theta_2 + \sin(\theta - \theta_1 + \theta_2) \\ &\quad + \gamma \sin \theta_2 + \gamma \sin(\theta - \theta_1 + \theta_2) \cos(\theta - \theta_1) \}^{-1} \\ &= \frac{\gamma_1^2}{|1 + \gamma \cos(\theta - \theta_1)|} = \frac{2\gamma_1^2}{|1 + \gamma_1^2 - \gamma^2|} = \frac{\gamma_1}{|\hat{\omega}'_2 \cdot \hat{v}'_2|}, \end{aligned}$$

giving us

$$\left| \frac{d\Omega_L(\theta_L, \phi_L)}{d\Omega(\theta, \phi)} \right|^{-1} = \frac{2\gamma_1^3}{|1 + \gamma_1^2 - \gamma^2|} = \frac{\gamma_1^2}{|\hat{\omega}'_2 \cdot \hat{v}'_2|}, \quad (\text{A8})$$

where $(\hat{\omega}'_2 \cdot \hat{v}'_2)$ is the cosine of the angle between the recoil velocities of particle 2 (CsX) in the c.m. and the laboratory frames, and the relation $\gamma^2 = 1 + \gamma_1^2 + 2 \cos(\hat{\omega}'_2 \cdot \hat{v}'_2)$ has been used to obtain the last form. The Jacobian, as was pointed out earlier, becomes infinite when either the recoil velocity of the alkali halide in the center-of-mass frame ω'_2 becomes very small, or when the recoil velocities of the alkali halide in the c.m. and the laboratory frames are perpendicular. Since the Jacobian, a transformation between two finite differential cross sections, cannot physically become infinite, a separate expression for it must be derived for the two cases cited above.

When one of the collision partners is initially stationary in the laboratory frame, i.e., $v_1 = 0$ and $\theta_1 = \theta_2 = 0$, this expression reduces to the one given by Schiff⁹

$$\begin{aligned} \left| \frac{d\Omega_L(\theta_L, \phi_L)}{d\Omega(\theta, \phi)} \right|^{-1} &= \left(\frac{(1 + \gamma^2 + 2\gamma \cos \theta)^{3/2}}{|1 + \gamma \cos \theta|} \right) \\ &= \frac{2\gamma_1^3}{|1 + \gamma_1^2 - \gamma^2|}. \end{aligned}$$

Figure 14 shows that a maximum (top figure) and a minimum (bottom figure) laboratory scattering angle exists when the recoil velocities of the alkali halide in the c.m. and the laboratory frames are perpendicular. This is further clarified in Fig. 15 which gives a plot of the c.m. scattering angle as a function of the laboratory scattering angle. This figure clearly displays the extrema in the laboratory scattering angle as a function of the c.m. scattering angle. At these extrema, the expression (A8) for the Jacobian becomes infinite. Figure 16 gives a plot of the laboratory recoil velocity of CsF as a function of the laboratory scattering angle. The laboratory recoil velocity displays an extremum at the minimum and maximum laboratory scattering angles. This is the reason that the absolute value of the Jacobian stays constant for large changes in the laboratory recoil velocity of CsF (Fig. 9). To derive an expression for the Jacobian when the recoil velocities of the alkali halide in the c.m. and the laboratory frames are perpendicular, one can write, using Fig. 17

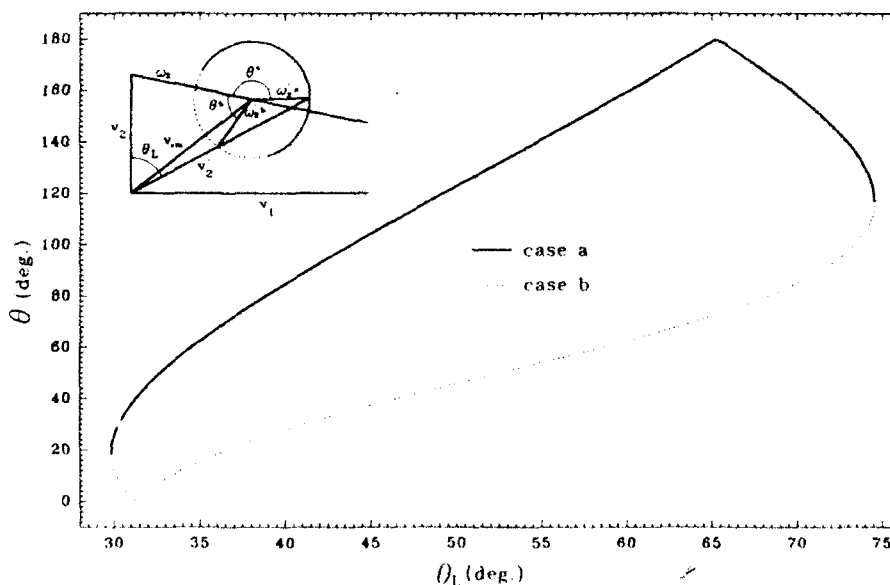


FIG. 15. Plot of the laboratory scattering angle θ_L as a function of the center of mass scattering angle θ for the $(v=3, j=80 \rightarrow v'=20, j'=118)$ transition of CsF ($v_1=2450$ m/s, $v_2=500$ m/s, $\Delta E/E=0.7778$, $\omega_2=246$ m/s, $v_{cm}=646$ m/s). It is seen that the laboratory scattering angle, for these collision parameters, cannot be less than about 30° and more than about 75° . The laboratory recoil velocity v'_2 and the c.m. recoil velocity ω'_2 are perpendicular for the maximum and minimum laboratory scattering angles and the laboratory scattering angle as a function of c.m. scattering angle displays an extremum. This leads to the display of rainbows in the curve of the laboratory differential cross section as a function of the laboratory recoil velocity at the maximum and minimum laboratory scattering angles. The discontinuities in the curve at c.m. scattering angles of 0° and 180° are not real and arise from the fact that the c.m. scattering angle is measured modulo π and not modulo 2π .

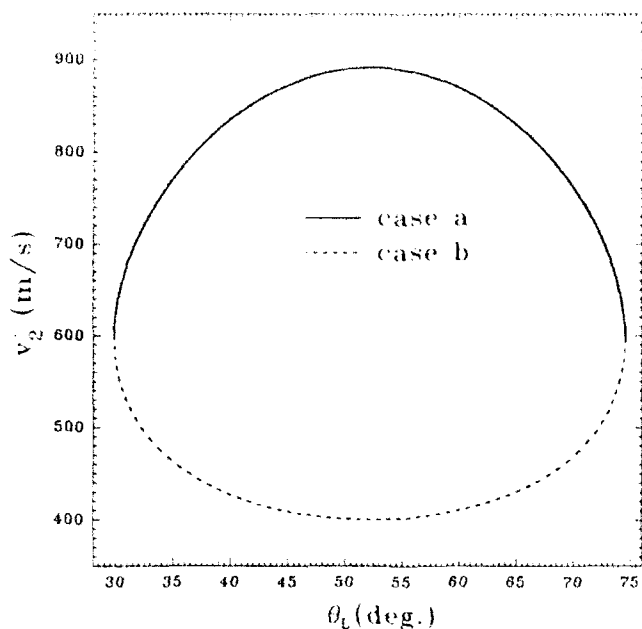


FIG. 16. Laboratory recoil velocity of CsF as a function of the laboratory scattering angle. The collision parameters are the same as in Fig. 15. At the rainbow angles, $v_{cm}^2 = (\omega_2')^2 + (v_2')^2$ and the laboratory recoil velocity of CsF is 597 m/s, slightly smaller than the velocity of the center of mass. When the laboratory scattering angle is not equal to the rainbow angles, the signal from each transition is observed at two recoil velocities, one lower and one higher than the velocity of the center of mass, corresponding to the cases *a* and *b* center of mass scattering angles. Both cases contribute to the ballistic peak.

$$\cos\left(\frac{\Delta\theta}{2}\right) \approx \left(\frac{\omega_2' - v_2'\Delta\theta_L}{\omega_2'}\right) \approx (1 - \gamma_1\Delta\theta_L) \quad (\text{A9})$$

or

$$\Delta\theta \approx 2 \arccos(1 - \gamma_1\Delta\theta_L). \quad (\text{A10})$$

Using the relations $\arcsin(x) + \arccos(x) = \pi/2$, and $\arcsin(1-x) \approx \pi/2 - (2x)^{1/2}$, we get

$$\left|\frac{\Delta\theta_L}{\Delta\theta}\right|^{-1} \approx \left|\frac{8\gamma_1}{\Delta\theta_L}\right|^{1/2}. \quad (\text{A11})$$

Together with

$$\left|\frac{d\phi_L}{d\phi}\right|^{-1} = \gamma_1 \left|\frac{\sin\theta_L}{\sin(\theta - \theta_1 + \theta_2)}\right|, \quad (\text{A12})$$

$$d\Omega = \sin(\theta - \theta_1 + \theta_2) d\theta d\phi,$$

and

$$d\Omega_L = \sin\theta_L d\theta_L d\phi_L,$$

we get,

$$\left|\frac{d\Omega_L}{d\Omega}\right|^{-1} \approx \left|\frac{8\gamma_1^3}{\Delta\theta_L}\right|^{1/2}. \quad (\text{A13})$$

When the laboratory recoil velocity is along the centroid velocity, one can write, using Fig. 13, $\theta = \theta_1$, and $\theta_2 = \theta_L$, giving

$$\left|\frac{d\Omega_L}{d\Omega}\right|^{-1} = \gamma_1^2. \quad (\text{A14})$$

This expression for the Jacobian is valid only when the laboratory recoil velocity is along the centroid velocity provided $\gamma_1\Delta\theta_L < 1$ and $\gamma_1\Delta\phi_L < 1$, $\Delta\theta_L$ and $\Delta\phi_L$ being the width of the laboratory detector in the polar and azimuthal angles. When this condition does not hold, the Jacobian becomes a constant and is simply equal to $4\pi/\Delta\Omega_L$. This is because the signal from all 4π steradians in the c.m. frame is now collected by the detector; a wider detector would not be able to collect any more signal.

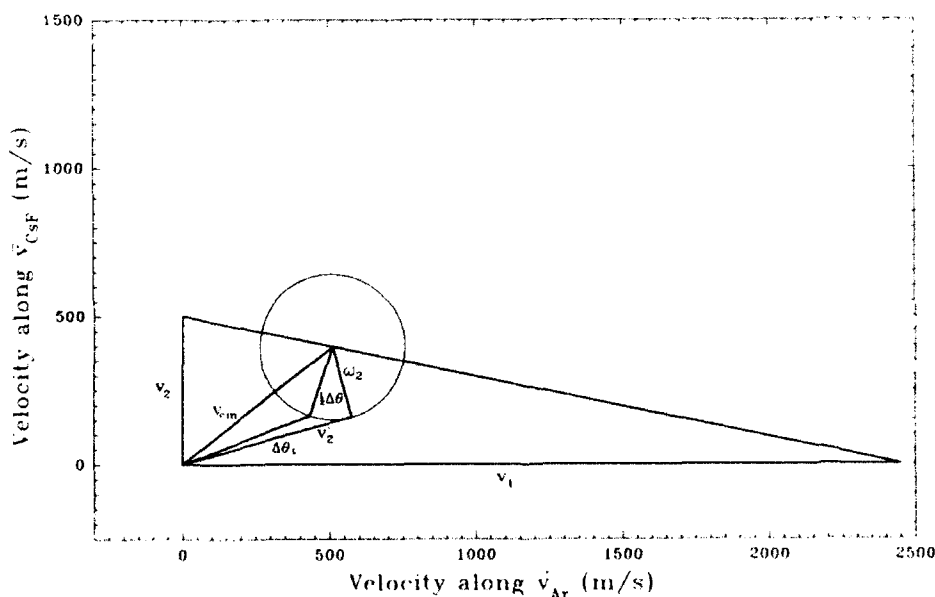


FIG. 17. Vector diagram illustrating the uncertainty in the c.m. scattering angle due to a small uncertainty in the laboratory scattering angle at the rainbow angle. The angular resolution of the detector, $\Delta\theta_L$, is exaggerated for the purpose of clarity.

To make the connection with the previous work,^{2,3} we start with Eq. (A8) and note that

$$\hat{\omega}'_2 \cdot \hat{v}'_2 = \frac{d\omega'_2}{dv'_2} \quad (\text{A15})$$

This equation is easy to prove. Using Fig. 13, we write

$$(\omega'_2)^2 = (v'_2)^2 + v_{c,m}^2 - 2v'_2 v_{c,m} \cos(\theta_L - \theta_2). \quad (\text{A16})$$

Differentiating Eq. (A16), we get

$$\omega'_2 d\omega'_2 = v'_2 dv'_2 - v_{c,m} dv'_2 \cos(\theta_L - \theta_2). \quad (\text{A17})$$

Substituting for $\cos(\theta_L - \theta_2)$ from Eq. (A16) we get Eq. (A15). Going back to Eq. (A8), when there is a continuous distribution of energy levels, the Jacobian becomes just γ_1^2 . In our case, since we are dealing with discrete quantized rotational-vibrational levels, the Jacobian is given by Eq. (A8).

¹H. J. Loesch and D. R. Herschbach, *J. Chem. Phys.* **57**, 2038 (1972).

²D. L. King, H. J. Loesch, and D. R. Herschbach, *Discuss. Faraday Soc.* **55**, II-34 (1973).

³D. L. King, Ph.D. thesis, Chemistry Department, Harvard University, 1974. The scattering angles in this reference are measured from the direction of the Ar beam, whereas in Refs. 1 and 2 they are measured from the direction of the cesium halide beam. We, in this work, will follow Refs. 1 and 2 and measure the angles from the cesium halide beam.

⁴J. M. Sindoni and R. D. Sharma, *Phys. Rev. A* **45**, R2659 (1992); J. M. Sindoni and R. D. Sharma, *J. Chem. Phys.* **97**, 737 (1992).

⁵S. W. Benson, G. C. Bernard, and James C. Wu, *J. Chem. Phys.* **38**, 25 (1963). See also S. W. Benson, *The Foundations of Chemical Kinetics* (McGraw-Hill, New York, 1960).

⁶R. D. Levine and R. B. Bernstein, *Molecular Reaction Dynamics and Chemical Reactivity*, 2nd ed. (Oxford University, New York, 1987).

⁷E. A. Entemann, Ph.D. thesis, Chemistry Department, Harvard University, 1967.

⁸T. T. Warnock and R. B. Bernstein, *J. Chem. Phys.* **49**, 1878 (1968).

⁹L. I. Schiff, *Quantum Mechanics* (McGraw-Hill, New York, 1968).

¹⁰M. S. Child, *Molecular Collision Theory* (Academic, London, 1974).

¹¹R. N. Zare, Ph.D. thesis, Chemistry Department, Harvard University, 1964.

¹²*Molecular Collision Dynamics*, edited by J. M. Bowman (Springer, New York, 1983), Chap. 4.

¹³R. D. Sharma, P. M. Bakshi, and J. M. Sindoni, *Phys. Rev. A* **43**, 189 (1991).

¹⁴J. M. Eisenberg and D. S. Kolton, *Theory of Meson Interactions with Nuclei* (Wiley-Interscience, New York, 1980).

¹⁵A. S. Davydov, *Quantum Mechanics* (Addison-Wesley, Reading, 1964).

¹⁶L. D. Landau and E. M. Lifshitz, *Mechanics* (Pergamon, New York, 1969).

¹⁷R. D. Sharma, P. M. Bakshi, and J. M. Sindoni, *Phys. Rev. A* **41**, 6540 (1990).

¹⁸R. D. Sharma and J. M. Sindoni, *Phys. Rev. A* **45**, 531 (1992).

¹⁹M. E. Rose, *Elementary Theory of Angular Momentum* (Wiley, New York, 1957).

²⁰J. O. Hirschfelder, C. F. Curtiss, and R. B. Bird, *Molecular Theory of Gases and Liquids* (Wiley, New York, 1954). The hard core radii obtained were: $r(\text{Ar}-\text{Cs}^+) = 3.8 \text{ \AA}$ and $r(\text{Ar}-\text{F}^-) = 3.1 \text{ \AA}$. However, to conform with the earlier work (Ref. 1) $r(\text{Ar}-\text{Cs}^+)$ was changed to 3.5 \AA.

²¹K. P. Huber and G. Herzberg, *Constants of Diatomic Molecules* (Van Nostrand Reinhold, New York, 1979).

²²In Ref. 4, v_1 , the velocity of Ar, was taken equal to 2550 m/s, the relative translational energy corresponding to this velocity is 1.1 eV. It was since deemed more likely, based on the parameters in Ref. 3, that the actual beam velocity peaked at 2450 m/s, corresponding to relative translational energy of 1.0 eV.

²³H. Dothe and R. D. Sharma (to be published)

Accession For	
NTIS	<input checked="" type="checkbox"/>
GRA&I	<input type="checkbox"/>
DTIC TAB	<input type="checkbox"/>
Unannounced	<input type="checkbox"/>
Justification	
By	
Distribution	
Availability Codes	
Avail and/or	
Dist	Special
A-1	20